Direct proteomic and high-resolution microscopy biopsy analysis identifies distinct ventricular fates in severe aortic stenosis

Sören Brandenburg [a,b,c,d,*], Lena Drews [b], Hanne-Lea Schönberger [b], Christoph F. Jacob [a,b], Nora Josefine Paulke [b], Bo E. Beuthner [a,c], Rodi Topci [a], Tobias Kohl [a,b], Lisa Neuenroth [e], Ingo Kutschka [f], Henning Urlaub [e,g,h], Fabian Kück [i], Andreas Leha [c,i], Tim Friede [c,i], Tim Seidler [a,c], Claudius Jacobshagen [j], Karl Toischer [a,c,d,k], Miriam Puls [a,c], Gerd Hasenfuß [a,b,c,d,k], Christof Lenz [d,e,g,k,l], Stephan E. Lehnart [a,b,c,d,h,k,l,*]

[a] Clinic of Cardiology & Pneumology, University Medical Center Göttingen, Germany
[b] Cellular Biophysics & Translational Cardiology Section, Heart Research Center Göttingen, University Medical Center Göttingen, Germany
[c] DZHK (German Centre for Cardiovascular Research), Partner Site Göttingen, Germany
[d] Collaborative Research Center SFB1002 "Modulatory Units in Heart Failure", University of Göttingen, Germany
[e] Department of Clinical Chemistry, University Medical Center Göttingen, Germany
[f] Clinic of Cardiothoracic & Vascular Surgery, University Medical Center Göttingen, Germany
[g] Bioanalytical Mass Spectrometry Group, Max Planck Institute for Multidisciplinary Sciences, Göttingen, Germany
[h] Collaborative Research Center SFB1190 "Compartmental Gates and Contact Sites in Cells", University of Göttingen, Germany
[i] Department of Medical Statistics, University Medical Center Göttingen, Germany
[j] Department of Cardiology, Intensive Care & Angiology, Vincentius-Diakonissen-Hospital Karlsruhe, Germany
[k] Cluster of Excellence "Multiscale Bioimaging: from Molecular Machines to Networks of Excitable Cells" (MBExC), University of Göttingen, Germany
[l] Leducq Transatlantic Network of Excellence CURE-PLaN, Clinic of Cardiology & Pneumology, University Medical Center Göttingen, Germany

ARTICLE INFO

ABSTRACT

The incidence of aortic valve stenosis (AS), the most common reason for aortic valve replacement (AVR), increases with population ageing. While untreated AS is associated with high mortality, different hemodynamic subtypes range from normal left-ventricular function to severe heart failure. However, the molecular nature underlying four different AS subclasses, suggesting vastly different myocardial fates, is unknown. Here, we used direct proteomic analysis of small left-ventricular biopsies to identify unique protein expression profiles and subtype-specific AS mechanisms. Left-ventricular endomyocardial biopsies were harvested from patients during transcatheter AVR, and inclusion criteria were based on echocardiographic diagnosis of severe AS and guideline-defined AS-subtype classification: 1) normal ejection fraction (EF)/high-gradient; 2) low EF/high-gradient; 3) low EF/low-gradient; and 4) paradoxical low-flow/low-gradient AS. Samples from non-failing donor hearts served as control. We analyzed 25 individual left-ventricular biopsies by data-independent acquisition mass spectrometry (DIA-MS), and 26 biopsies by histomorphology and cardiomyocytes by STimulated Emission Depletion (STED) superresolution microscopy. Notably, DIA-MS reliably detected 2273 proteins throughout each individual left-ventricular biopsy, of which 160 proteins showed significant abundance changes between AS-subtype and non-failing samples including the cardiac ryanodine receptor (RyR2). Hierarchical clustering segregated unique proteotypes that identified three hemodynamic AS-subtypes. Additionally, distinct proteotypes were linked with AS-subtype specific differences in cardiomyocyte hypertrophy. Furthermore, superresolution microscopy of immunolabeled biopsy sections showed subcellular RyR2-cluster fragmentation and disruption of the functionally important association with transverse tubules, which occurred specifically in patients with systolic dysfunction and may hence contribute to depressed left-ventricular function in AS.

1. Introduction

Aortic valve stenosis (AS) represents *the* most common valvular heart disease and a major cause of heart failure. AS is highly prevalent in 4–5% of the general population from 65 years or older, rising drastically at higher ages [3–6]. Once severe and symptomatic, treatment of AS requires prosthetic aortic valve replacement (AVR) [7]. While valvular calcification and degeneration develop slowly over years, progressive obstruction of left-ventricular outflow induces myocardial remodeling and dysfunction. Morbidity and outcome are, thus, determined by a synergistic downward spiral between AS severity *and* left-ventricular dysfunction. Symptomatic severe AS causes a 1-year mortality approaching 50% [8]. Hence, current guidelines recommend AVR for all patients with severe AS (defined as aortic valve area ≤ 1 cm^2) who are either symptomatic *or* have developed left-ventricular dysfunction [1,2].

While the mechanisms leading from compensatory left-ventricular hypertrophy in AS to symptomatic heart failure remain incompletely understood, different hemodynamic subtypes were recently introduced based on left-ventricular structural and functional −systolic or diastolic− echocardiographic changes [1,2]. A critical loss of myocytes and increasing myocardial fibrosis may in part explain the transition from adaptive hypertrophy to left-ventricular ejection fraction (LVEF) depression in severe AS [9,10]. Whereas gross replacement fibrosis is presumably irreversible, functionally relevant, cardiomyocyte-specific proteomic and mechanistic biomarkers of particular AS-subtypes remain ill defined. Importantly, differentiation of AS-subtypes based on new proteomic biomarkers is not only relevant to dissect different molecular left-ventricular disease pathomechanisms, but may trigger new precision therapy concepts beyond the current empirical, guideline-biased AS-subtype classification [1,2].

Rapidly emerging faster, deeper mass spectrometry (MS) techniques demonstrated the first proteomic mapping of atrial and ventricular tissues in a small number of human hearts [11]. Moreover, MS has been applied to study cardiac diseases including AS previously [12–14]. Recently, quantitative techniques for deep proteomic profiling of small tissue samples by data-independent acquisition mass spectrometry (DIA-MS) were established [15]. Here, we extend DIA-MS for direct proteomic analysis of transcatheter left-ventricular biopsies for the first time. Specifically, we investigate the hypothesis that unique proteomic profiles identify specific hemodynamic AS-subtypes in individual biopsy samples from patients undergoing transcatheter AVR.

Indeed, proteomic analyses identified AS-subtypes with distinctive protein abundance profiles, hereafter referred as 'proteotypes'. Quantitative proteomic profiling consistently detected 2273 proteins across all samples, of which 160 proteins showed significant differential abundance changes and tightly clustered with three hemodynamic AS-subtypes. Importantly, these proteotype changes affect essential cardiomyocyte functions, including, but not limited to, energy and redox metabolism, myofilament function, ion transport, and excitation-contraction (EC) coupling. EC *un*-coupling has been established previously as a central pathomechanism in heart failure [16–18]. However, EC *un*-coupling mechanisms have not been investigated comparatively between different AS-subtypes. Thus, we investigated the cardiomyocyte-specific disorganization of Ca^{2+} release units by superresolution microscopy in situ in endomyocardial biopsies. Finally, the subcellular cardiomyocyte and echocardiographic changes were analyzed by univariate regression modeling, demonstrating significant AS-subtype specific pathomechanistic correlations.

2. Methods

2.1. Study population

A total of 38 patients with symptomatic severe AS underwent transfemoral transcatheter AVR (TAVR) in the Clinic of Cardiology & Pneumology, University Medical Center Göttingen. The indication for TAVR was based on heart team consensus according to current guidelines [2], and valve implantation was performed using standard techniques. This study was designed as an exploratory discovery trial for analysis of proteome-wide abundance changes in cardiac biopsies by unbiased DIA-MS approaches. The procedures used in this study adhere to the tenets of the Declaration of Helsinki. The institutional review board (i.e., the ethics committee) approved the study (no. 10/5/16), and written informed consent was obtained from all patients.

2.2. Echocardiography

Pre-interventional echocardiography measurements were performed using either a Philips ie33 or a Philips Epiq7 system based on guideline recommendations [19]. Data were recorded in a Picture Archiving and Communication System, and retrospectively re-evaluated by a single observer (M.P.) using Q Station 3.8.5 (Philips healthcare). According to current guidelines [1,2] and as described previously [20], four distinct hemodynamic subtypes of severe AS were defined in the selected AS patient group:

(1) Normal/preserved ejection fraction, high-gradient AS (NEF-HG): aortic valve area (AVA) ≤ 1.0 cm^2, $V_{max} \geq 4$ m/s or $\Delta P_m \geq 40$ mmHg, and LVEF $\geq 50\%$.

(2) Low/reduced ejection fraction, high-gradient AS (LEF-HG): AVA ≤ 1.0 cm^2, $V_{max} \geq 4$ m/s or $\Delta P_m \geq 40$ mmHg, and LVEF $< 50\%$.

(3) Low/reduced ejection fraction, low-gradient AS ('classic' low-flow, low-gradient AS) (LEF-LG): AVA ≤ 1.0 cm^2, $V_{max} < 4$ m/s and $\Delta P_m < 40$ mmHg, LVEF $< 50\%$, and stroke volume index (SVI) ≤ 35 mL/m^2.

(4) Paradoxical low-flow, low-gradient AS (PLF-LG): AVA ≤ 1.0 cm^2 and indexed AVA ≤ 0.6 cm^2/m^2, $V_{max} < 4$ m/s and $\Delta P_m < 40$ mmHg, LVEF $\geq 50\%$, and SVI ≤ 35 mL/m^2.

2.3. Endomyocardial left-ventricular biopsy processing

Following TAVR, left-ventricular biopsies were obtained from the basal anteroseptum using biopsy forceps (Proflex-Bioptom 7F, Medical Imaging Systems) [20], snap-frozen in liquid nitrogen for mass spectrometry, and fixed in 4% paraformaldehyde for histologic, confocal and superresolution STED microscopy [21]. The graphical abstract summarizes the standardized proteomic and imaging workflows. Left-ventricular biopsies from human non-failing donor hearts rejected for transplantation served as control. Due to the invasive nature of biopsy sampling, the number of precious left-ventricular biopsies was limited by the use & access committee of the University Medical Center Göttingen. However, at least $n = 5$ left-ventricular biopsies per AS-subtype could be included in all analyses.

2.4. Unbiased mass spectrometry-based proteotype profiling

A new standardized protocol for sample preparation of left-ventricular biopsies was developed (detailed in the Supplementary Information). Five human left-ventricular biopsies per AS or control group, representative of individual patients, were lysed and tryptically digested by pressure cycling (Barocycler 2320 EXT, Pressure Biosciences). Following desalting, an annotated MS/MS spectral library was generated from a fractionated pooled sample by data-dependent acquisition mass spectrometry using a Top20 method on a hybrid quadrupole/time-of-flight mass spectrometer (TripleToF 5600+, Sciex). This library comprises 43,439 human peptide sequences representing 2951 proteins, each at 1% FDR. For quantitative proteomic profiling, individual patient samples were analyzed in injection duplicate by DIA-MS using a 65 Variable Window acquisition method on the same instrument. Following retention time calibration, precursor-to-fragment ion chromatograms for the precursors in the library were extracted at

an FDR of 1%, and combined at the peptide and protein levels. Proteome profiles were normalized using Total Area Sums for comparative analysis. Protein quantifications were log-transformed and quantile-normalized between all samples (Supplementary Fig. 1).

2.5. Superresolution STED nanoscopy

Left-ventricular biopsies fixed in 4% paraformaldehyde were embedded in paraffin and cut into 5 μm sections for histology. For immuno- or customized WGA-fluorescence labeling of deparaffinized and rehydrated samples, antigens were unmasked in sodium-citrate buffer prior to antibody or WGA incubation (procedures as described in Supplementary Information). Samples were blocked and permeabilized with 4% BSA and 0.1% Triton-X100. Dual-color STED imaging used a customized laser-scanning microscope (TCS SP8, Leica) with a 100×/1.40 oil objective (HC PL APO C2S). Raw images were processed in Fiji (https://imagej.net/Fiji). Quantitative image analysis included signal segmentation based on previously published protocols (Supplementary Information) [21–23].

2.6. Statistical analysis

Data are represented as mean ± SEM if not stated otherwise. Box-plots indicate the median and the interquartile range, and whiskers represent the 5th and 95th percentiles. Data plotting and statistical analyses were performed in GraphPad Prism 7.03, Microsoft Excel 2010, Origin-Pro 8.5G, Perseus 1.6.14.0, SPSS Statistics 28.0.1.1, and R version 3.4.0 and 3.6.1 (including the R-package SIMEX, version 1.8) [24,25]. Statistical hypothesis tests are specified in the figure legends and the Supplementary Information. Results in the proteomic analyses were adjusted for multiple testing using Benjamini-Hochberg to control the FDR. Due to the exploratory nature of this study, no adjustment for multiple testing was done in the other analyses. P values < 0.05 were accepted to indicate statistical significance.

3. Results

3.1. Proteomic profiling of left-ventricular endomyocardial biopsies from individual patients

To establish a mass spectrometry workflow for small left-ventricular endomyocardial patient samples (i.e., biopsies weighing 4–7 mg), we further developed the protocol by Guo et al. for tissue lysis of individual biopsies (i.e., one per AS patient) using pressure cycling technology and DIA-MS [15]. (See Supplementary Information for detailed descriptions.) Following informed consent, left-ventricular biopsies from the basal anteroseptum were obtained from patients with symptomatic severe AS following TAVR. Based on echocardiographic classification of four distinct hemodynamic AS-subtypes (Fig. 1A; refer to Supplementary Tables 1 and 2 for detailed clinical information), twenty biopsy samples representing each hemodynamic AS-subtype were processed for quantitative analyses by DIA-MS (total n = 20; n = 5 each for NEF-HG, LEF-HG, LEF-LG, and PLF-LG). In addition, five biopsies from non-failing (NF) explanted human hearts were used as control. Based on two replicate injections per patient sample, DIA-MS reproducibly quantified 2273 proteins across all samples, of which 160 proteins showed statistically significant abundance changes between the different AS-subtypes and NF control samples (Online Source 1).

Principal component analysis segregated AS-subtypes from NF control samples, and suggested a clustering of the AS-subtypes LEF-LG, PLG-LG, and NEF-HG (Fig. 1B). Only LEF-HG samples were mapped in different subgroups on the principal component analysis plot, clustering with or next to other AS subtypes (Fig. 1B, *blue*). Hierarchical clustering segregated three distinct AS proteotypes between the 160 differentially abundant proteins: LEF-LG, PLF-LG, and NEF-HG (Fig. 1C). Additionally, tight clustering of replicates confirmed a high degree of technical

reproducibility (Fig. 1C), which is supported by an overall high DIA-MS data quantification correlation between the two technical replicates (Supplementary Fig. 2). Hence, we identified three unique AS proteotypes by an unsupervised approach, which correspond to specific echocardiographic AS-subtypes and current clinical guidelines [1,2]. Despite a preserved systolic left-ventricular function, both the NEF-HG and PLF-LG proteotypes showed the greatest Euclidean distance from NF (Fig. 1C).

In sharp contrast, LEF-HG samples showed more variable proteotype patterns, clustering in two separate subgroups designated LEF-HG-a and LEF-HG-b (Fig. 1C, *blue*). Interestingly in LEF-HG, LVEF ranged from 17% to 47% (Supplementary Fig. 3A). While the LEF-HG-a proteotype (LVEF ≤30%) was closely associated with LEF-LG (Fig. 1C, IDs 1, 4 and 5), the LEF-HG-b proteotype (LVEF > 45%) clustered with NEF-HG (Fig. 1C, IDs 2 and 3). These results support two distinct proteotypes possibly explained by transitory LEF-HG phenotypes as indicated by the broader LVEF variability. Coloration of the principal component analysis plot based on the patients' LVEF values explicitly demonstrated the relevance of left-ventricular systolic function for LV biopsy sample clustering (Supplementary Fig. 3B). To verify the number of proteotypes segregated in individual clusters, we applied the bioinformatic tools ConsensusClusterPlus and NbClust (Supplementary Fig. 4–5, Supplementary Table 4) [26,27]. Although our data do not show one exact small number of clusters due to the biological variance in human left-ventricular biopsies, three clusters reflecting the AS proteotypes LEF-LG, PLG-LG, and NEF-HG seemed to be reasonable (Supplementary Fig. 4–5, Supplementary Table 4).

To further explore our proteomic results, we summarized the top 10 up- and downregulated proteins compared to NF, including singular or parallel subgroup changes (Fig. 1D). In addition, gene set enrichment analysis by Gene Ontology (GO) terms [28] for differential protein changes between AS-subtypes and NF highlights the most affected biological processes (Fig. 1E, Supplementary Fig. 6). GO term analysis implicates significant remodeling of the cardiac contractile apparatus and a reduced capacity for ATP synthesis via oxidative phosphorylation, indicating mitochondrial dysfunction. These processes have been linked to cardiomyopathy-associated diseases, particularly atrial fibrillation and aortic valve stenosis previously [11,12,14].

As patients enrolled in this proteomic study showed frequently observed AS comorbidities like coronary artery disease (CAD) and atrial fibrillation (AF) (Supplementary Tables 1–2), we wondered if the proteomic data may reveal differentially abundant proteins in the CAD vs. no CAD, or AF vs. no AF comparison, respectively. Therefore, the top 100 regulated proteins in the CAD/AF comparisons were analyzed by hierarchical clustering and presented in a heat map (Supplementary Fig. 7). While unsupervised hierarchical clustering reasonably segregated no CAD from CAD biopsies (Supplementary Fig. 7A), the AF vs. no AF comparison did not result in distinct clusters (Supplementary Fig. 7B). Importantly, none of the top 100 regulated proteins remained statistically significant after adjusting for multiple testing, and no GO term or KEGG pathway was significantly overrepresented in absence vs. presence of CAD or AF, respectively. Hence, in contrast to the differences seen between AS-subtypes and NF samples (Fig. 1C), the CAD and AF comparisons do not show a substantial impact on sample clustering (also see 5.5. Study limitations).
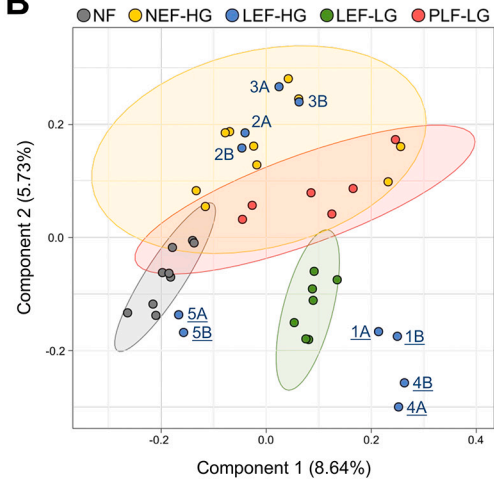
3.2. Gene Ontology term analysis in severe aortic stenosis proteotypes

Most interestingly, hierarchical clustering among the 160 differentially abundant proteins in Fig. 1C *right* segregated four clusters, which represent up- or downregulated proteins in one or more specific proteotypes (clusters i-iv), e.g. upregulated in PLF-LG (cluster ii). We applied gene set enrichment analyses by overrepresented GO terms and designed gene-concept-networks to study the biological processes regulated in severe AS proteotypes (Fig. 2). Whereas protein N-linked glycosylation is altered in AS except LEF-LG/LEF-HGa (cluster i, Fig. 2A-
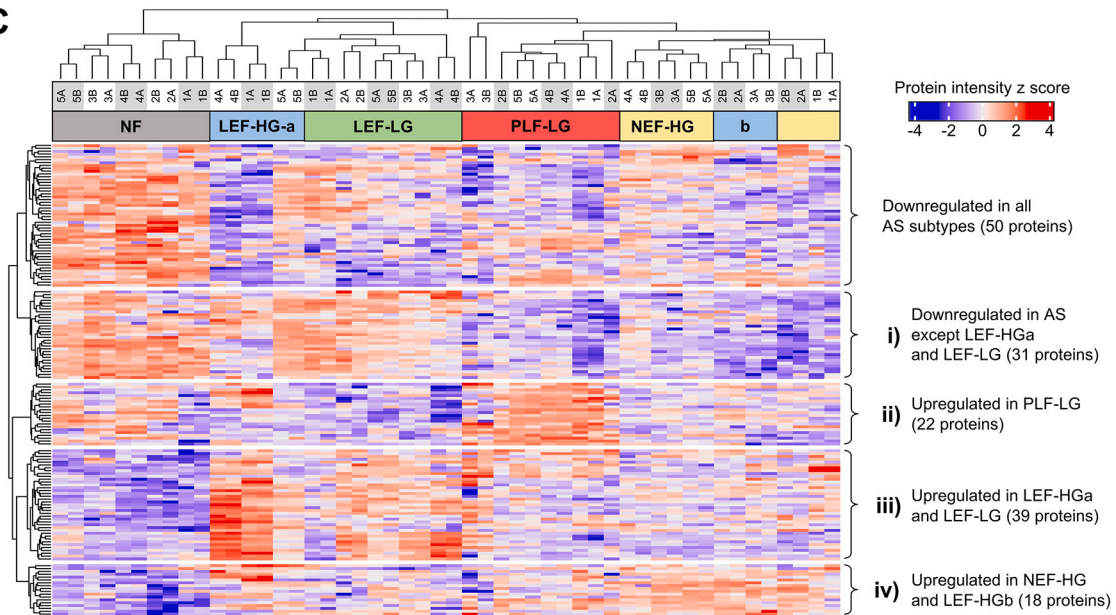
A

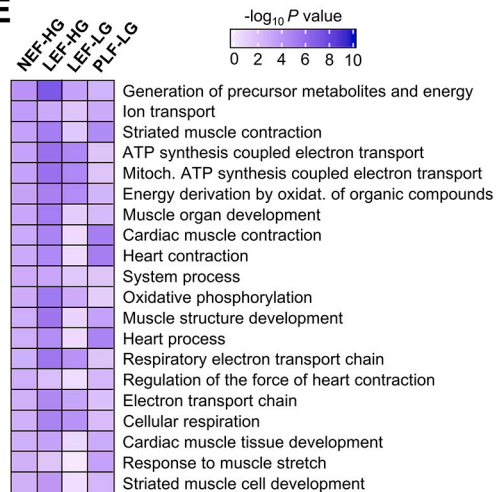| Echo	NEF-HG	LEF-HG	LEF-LG	PLF-LG
count (n)	5	5	5	5
AVA (cm²)	0.60 ± 0.05	0.60 ± 0.05	0.81 ± 0.08	0.78 ± 0.05
AVA/BSA (cm²/m²)	0.31 ± 0.03	0.29 ± 0.02	0.41 ± 0.04	0.40 ± 0.03
Vmax (m/s)	4.67 ± 0.18	4.16 ± 0.04	3.08 ± 0.17*,†	3.34 ± 0.13*,†
ΔPm (mmHg)	53.40 ± 4.18	53.40 ± 4.18	23.00 ± 2.64*,†	23.80 ± 1.91*,†
LVEF (%)	61.08 ± 3.86	32.36 ± 5.45*	32.38 ± 2.70*	57.10 ± 2.02†,‡
SVI (ml/m²)	35.69 ± 3.27	30.74 ± 2.16	29.85 ± 2.24	29.46 ± 0.98

B

Component 2 (5.73%) vs Component 1 (8.64%)

NF, NEF-HG, LEF-HG, LEF-LG, PLF-LG

C

Protein intensity z score: −4 −2 0 2 4

NF | LEF-HG-a | LEF-LG | PLF-LG | NEF-HG | b

Downregulated in all AS subtypes (50 proteins)

i) Downregulated in AS except LEF-HGa and LEF-LG (31 proteins)

ii) Upregulated in PLF-LG (22 proteins)

iii) Upregulated in LEF-HGa and LEF-LG (39 proteins)

iv) Upregulated in NEF-HG and LEF-HGb (18 proteins)

D

	NEF-HG	LEF-HG	LEF-LG	PLF-LG
1	CRYM	ST13	TGM2	CRYM
2	ST13	HSPB2-C11orf52	ACTN1	CTSD
3	SYNPO2L	TGM2	VTN	ST13
4	TGM2	ACTN1	VCAN	VTN
5	HSPE1	SYNM	RNASE4	CRYAB
6	IDH3A	NES	POSTN	HSPB2-C11orf52
7	HSPB2-C11orf52	CRYM	MYL9	SOD2
8	HSPB1	MYL12A	DES	CA2
9	SYNM	SYNPO2L	MYL12A	ACADSB
10	GRPEL1	PPIA	COL18A1	FHL1
1	SLC25A3	SRL	SRL	SRL
2	NDUFB5	NDUFB5	ME2	SLC25A12
3	SLC25A12	SLC25A3	NDUFB8	PYGM
4	EHD2	MT-CO2	MYH6	SLC25A3
5	DDOST	ATP2A2	MB	NDUFA9
6	ME2	ME2	DSTN	RPS9
7	MT-CO2	MYH6	NDUFAB1	MT-CO2
8	RPN1	CD36	TMEM109	NNT
9	NDUFB8	NDUFB8	ACAT1	EHD2
10	RPS9	SLC25A12	COX6A2	MYH6

E

−log₁₀ P value: 0 2 4 6 8 10

Columns: NEF-HG, LEF-HG, LEF-LG, PLF-LG

Generation of precursor metabolites and energy
Ion transport
Striated muscle contraction
ATP synthesis coupled electron transport
Mitoch. ATP synthesis coupled electron transport
Energy derivation by oxidat. of organic compounds
Muscle organ development
Cardiac muscle contraction
Heart contraction
System process
Oxidative phosphorylation
Muscle structure development
Heart process
Respiratory electron transport chain
Regulation of the force of heart contraction
Electron transport chain
Cellular respiration
Cardiac muscle tissue development
Response to muscle stretch
Striated muscle cell development

(caption on next page)

Fig. 1. Expression profiling of individual left-ventricular patient biopsies identifies proteotype-specific aortic stenosis phenotype clusters. (A) Based on recent echocardiography criteria [1,2], patients diagnosed with severe AS (AVA < 1.0 cm²) were sub-classified into four hemodynamic subgroups for subsequent proteomic analysis. The table confirms typical hemodynamic subgroup characteristics for NEF-HG, LEF-HG, LEF-LG, and PLF-LG (each $n = 5$ patients). AVA, aortic valve area; AVA/BSA, body surface area; Vmax, peak aortic valve velocity; ΔPm, mean aortic valve pressure gradient; LVEF, left-ventricular ejection fraction; SVI, stroke volume index. Mean ± SEM, * P value of < 0.05 vs. NEF-HG; † P value of < 0.05 vs. LEF-HG; ‡ P value of < 0.05 vs. LEF-LG, one-way ANOVA with post-hoc Tukey test. (B-E) Label-free DIA-MS analysis of individual LV biopsies from the AS patients summarized in A. One LV biopsy per patient was processed by barocycling and analyzed through two technical replicates by DIA-MS. (B) Principal component analysis representing single LV biopsy samples from individual patients and non-failing (NF) controls. *Top:* Figure legend. Each circle projects individual patient sample data onto component 1 and 2, with the percentage of total variance listed in parentheses (x/y axis legend). Ellipses indicate the 95% confidence intervals. Each patient data set is represented by two technical replicates. Outlying replicates were excluded from this plot (1 NF, 3 LEF-LG, 4 PLF-LG). (C) *Top:* Unsupervised hierarchical clustering segregates all AS proteotype subgroups from the NF control group; and identifies each LEF-LG, PLF-LG, and NEF-HG as unique proteotype clusters. In contrast, the LEF-HG proteotypes are further segregated into two subclusters (a, b). *Bottom:* Heat map visualizing 160 protein intensities as differential abundances defined by the red-to-blue color table z score (ANOVA, FDR <0.05). Technical replicates are indicated on top by A/B. *Left and Right:* Among the differential abundant proteins, clusters i-iv) indicate proteins up- or downregulated in one or more AS subgroups further analyzed in Fig. 2. (D) Table summarizing each ten most up(↑)- or down(↓)-regulated proteins compared to non-failing samples. Grey versus white fields indicate proteins regulated in ≤2 versus ≥3 AS-subtypes. (E) Heat map representing highly regulated Gene Ontology terms identified by -$\log_{10}$ P value (look-up-table) and sorted by most increased in subgroup NEF-HG (top-to-bottom). Each represented biological process was significantly enriched in AS compared to non-failing samples. (For interpretation of the references to color in this figure legend, the reader is referred to the web version of this article.)-

◄━━━━━━━━━━━━━━━━━

B), PLF-LG showed changes in the GO terms intermediate filament and extracellular structure organization, and bicarbonate transport (cluster ii, Fig. 2C-D). In contrast, twelve GO terms related to nucleoside/nucleotide metabolism, cellular detoxification, and metabolism of sugars were overrepresented in NEF-HG/LEF-HGb (Fig. 2G-H). In addition, the clusters i-iv highlighted in Fig. 1C *right* were used to assess overrepresented KEGG pathways changed in severe AS proteotypes (Supplementary Fig. 8) [29].

3.3. Functionally relevant AS-subtype specific protein changes

Pairwise comparisons between the three segregated AS proteotype clusters versus NF revealed additional, functionally relevant protein changes. Firstly, both essential intracellular Ca²⁺ release versus uptake pathways of the sarcoplasmic reticulum (SR), RyR2 and SERCA2a (*ATP2A2*), respectively, were significantly down-regulated in NEF-HG (Fig. 3A). In addition, the Na⁺/K⁺-ATPase α1 subunit (*ATP1A1*) was downregulated, whereas troponin-T (*TNNT2*) was increased (Fig. 3A). Finally, dysferlin (*DYSF*) and clathrin heavy chain-1 (*CLTC*), with important membrane repair functions, were decreased in NEF-HG (Fig. 3A). Secondly, systolic heart failure in LEF-LG was specifically associated with a periostin (*POSTN*) increase, indicating active fibro-proliferative processes [30], and collagen accumulation (*COL18A1*) (Fig. 3B). Conversely, myoglobin (*MB*), the primary iron- and oxygen-binding protein of striated muscles, was specifically decreased in LEF-LG (Fig. 3B). Thirdly, specific for PLF-LG, lactate dehydrogenase B (*LDHB*) and superoxide dismutase-2 (*SOD2*) were significantly upregulated, highlighting key changes in cardiac energy or mitochondrial redox metabolism, respectively (Fig. 3C). In contrast, the muscle-specific glycogen phosphorylase 2 (*PYGM*) was decreased, suggesting increased lactate at the cost of depressed glycogen utilization in PLF-LG (Fig. 3C).

In Fig. 3D-F, proteomic differences between AS subtypes are illustrated. Compared to NEF-HG, collagen type IV α1 and α2 (*COL4A1* and *COL4A2*), the clathrin heavy chain-1 (*CLTC*), and the giant protein titin (*TTN*) were significantly increased in LEF-LG (Fig. 3D). Notably, comparing PLF-LG versus LEF-LG revealed the highest number of differentially changed proteins between any two AS subtypes (Fig. 3F): while *MB*, *SOD2*, creatine kinase B (*CKB*), and the phosphor-adaptor protein 14–3–3-epsilon (*YWHAE*) were markedly increased, glycogen debranching enzyme (*AGL*), myosin heavy chain 7B (*MYH7B*), and the chaperone calnexin (*CANX*) were significantly decreased. (Online Sources 2–11 provide all the statistically significant protein abundance changes that were identified in the ten pairwise comparisons between different AS subtypes and NF control samples.)

Finally, markedly different AS-subtype abundances are identified in the DIA-MS data for three important proteins. Essential for energy metabolism, the muscle-specific creatine kinase (*CKM*) was significantly

decreased in LEF-LG (EF < 50%), but unchanged in NEF-HG and PLF-LG with preserved left-ventricular function (Fig. 3G). Interestingly, like other collagens, collagen-α1 (XVIII) was selectively increased only in LEF-HG and LEF-LG (Fig. 3H). Importantly, the RyR2 Ca²⁺ release channel was significantly decreased in NEF-HG and LEF-HG, whereas LEF-LG and PLF-LG showed a tendency towards reduced RyR2 protein abundance (Fig. 3I). Hence, quantitative proteomic profiling of left-ventricular biopsies revealed AS-subtype specific, differential protein abundance changes, including, but not limited to, energy and redox metabolism, myofilament function, ion transport, and extracellular collagen.

Interestingly, correlation analysis of the 160 significantly regulated proteins with important echocardiography parameters showed a pronounced negative correlation of protein abundance with LVEF, and a pronounced positive correlation with the left-ventricular end-diastolic diameter (LVEDD) (Supplementary Fig. 9, Online Source 12). Comparison of *Pearson* correlation coefficients for this group of proteins revealed an inverse relationship, i.e. protein abundances that correlated negatively with LVEF function correlated positively with LVEDD and vice versa, further supporting strong interrelations between the proteotype and AS-subtype spectrum (Supplementary Fig. 9).

3.4. Histomorphology confirms distinct AS phenotypes

To further dissect subtype-specific AS differences in situ, we analyzed 21 additional endomyocardial biopsies and 5 NF samples by conventional and high-resolution histomorphology (see Supplementary Table 3 for clinical information). Despite severe AS, Hematoxylin-Eosin (HE) staining showed major differences in the extent of cardiomyocyte hypertrophy, ranked in the order NEF-HG > LEF-HG > LEF-LG > PLF-LG > NF (Fig. 4A). Furthermore, perinuclear lipofuscin deposits were most prominent in PLF-LG, but much less in other AS-subtype samples (Fig. 4A). To quantify the extent of cardiomyocyte changes, we used a custom-made wheat germ agglutinin (WGA) fluorescence staining, clearly delineating cardiomyocyte surface boundaries (Fig. 4B). Furthermore, WGA identified intracellular transverse-axial tubule (TAT) endomembrane structures (analyzed in Fig. 5). Finally, lipofuscin autofluorescence imaging [31] was used to quantify lipofuscin deposition (Fig. 4C, Supplementary Fig. 10). The former analysis revealed highly significant increases in cardiomyocyte cross-section area and maximal diameter in NEF-HG versus NF *and* PLF-LG, and in LEF-HG the cross-section area and maximal diameter were significantly increased compared to NF (Fig. 4D-E). As expected, analysis of binarized lipofuscin images confirmed a significant increase in perinuclear deposition in PLF-LG but not in other AS-subtypes (Fig. 4F). Of note, cardiomyocyte cross section area and lipofuscin deposition were directly or inversely correlated with AS peak flow velocity, respectively (Fig. 4G-H). Hence, in addition to proteomic differences, previously unknown AS-subtype
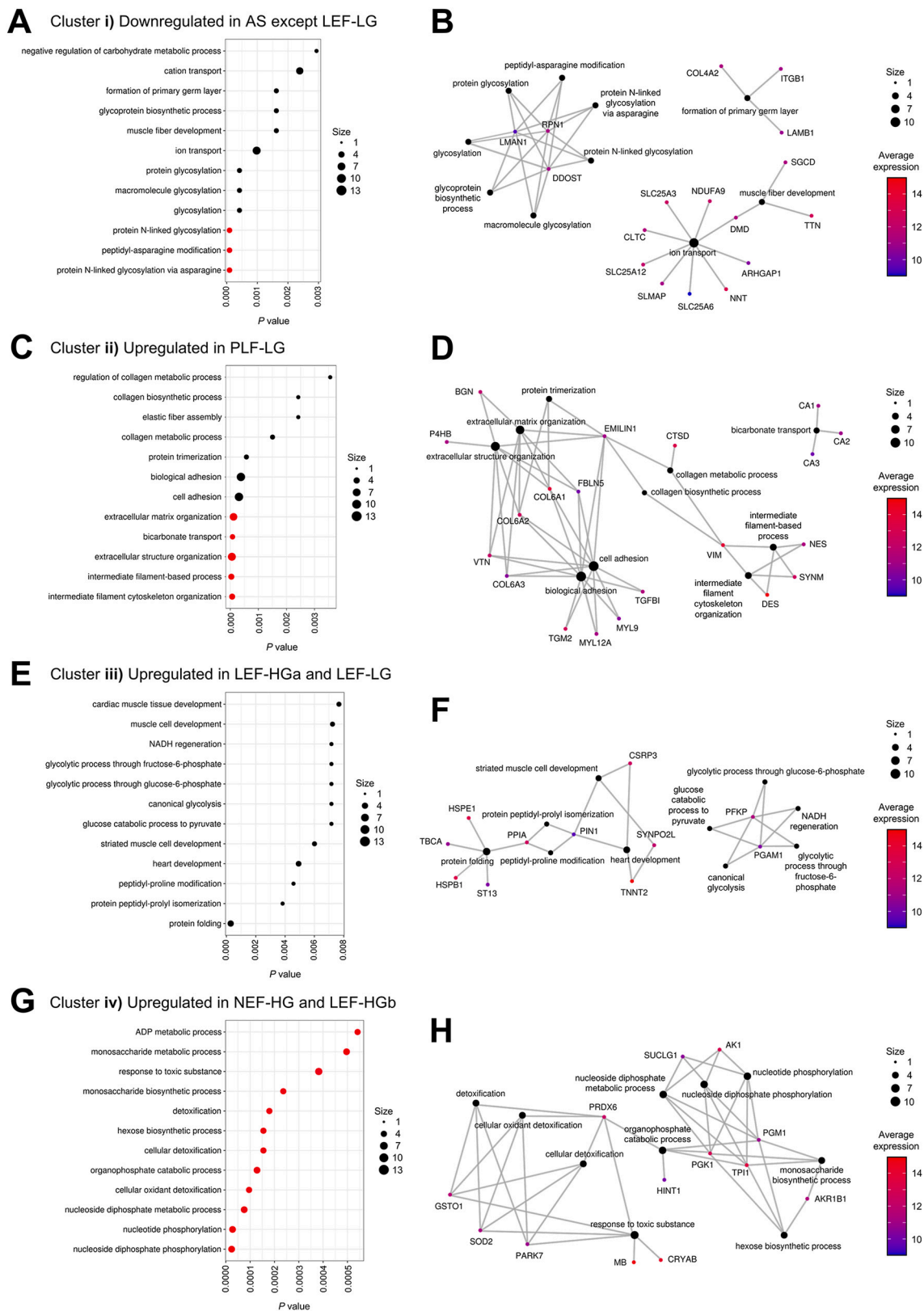
Fig. 2. Overrepresented Gene Ontology terms in clusters among differentially abundant proteins. (A-H) Unsupervised hierarchical clustering among the 160 differentially abundant proteins revealed clusters i-iv), representing up- or downregulated proteins in specific AS proteotypes (LEF-HGa/LEF-LG, PLF-LG, NEF-HG/LEF-HGb; compare Fig. 1C), which were further subjected to biological process Gene Ontology (GO) term analysis. (A, C, E, G) Tables summarizing the twelve most overrepresented GO terms in clusters i-iv). Red circles indicate GO terms remaining significantly overrepresented after adjusting for multiple testing. The circle size indicates the number of proteins linked to each GO term (figure legend). (B, D, F, H) Corresponding gene-concept-networks of the ten most overrepresented GO terms. The circle size indicates the number of proteins linked to each GO term (figure legend). Colors of the smaller protein circles point out the average protein abundance (blue-to-red LUT). (For interpretation of the references to color in this figure legend, the reader is referred to the web version of this article.)
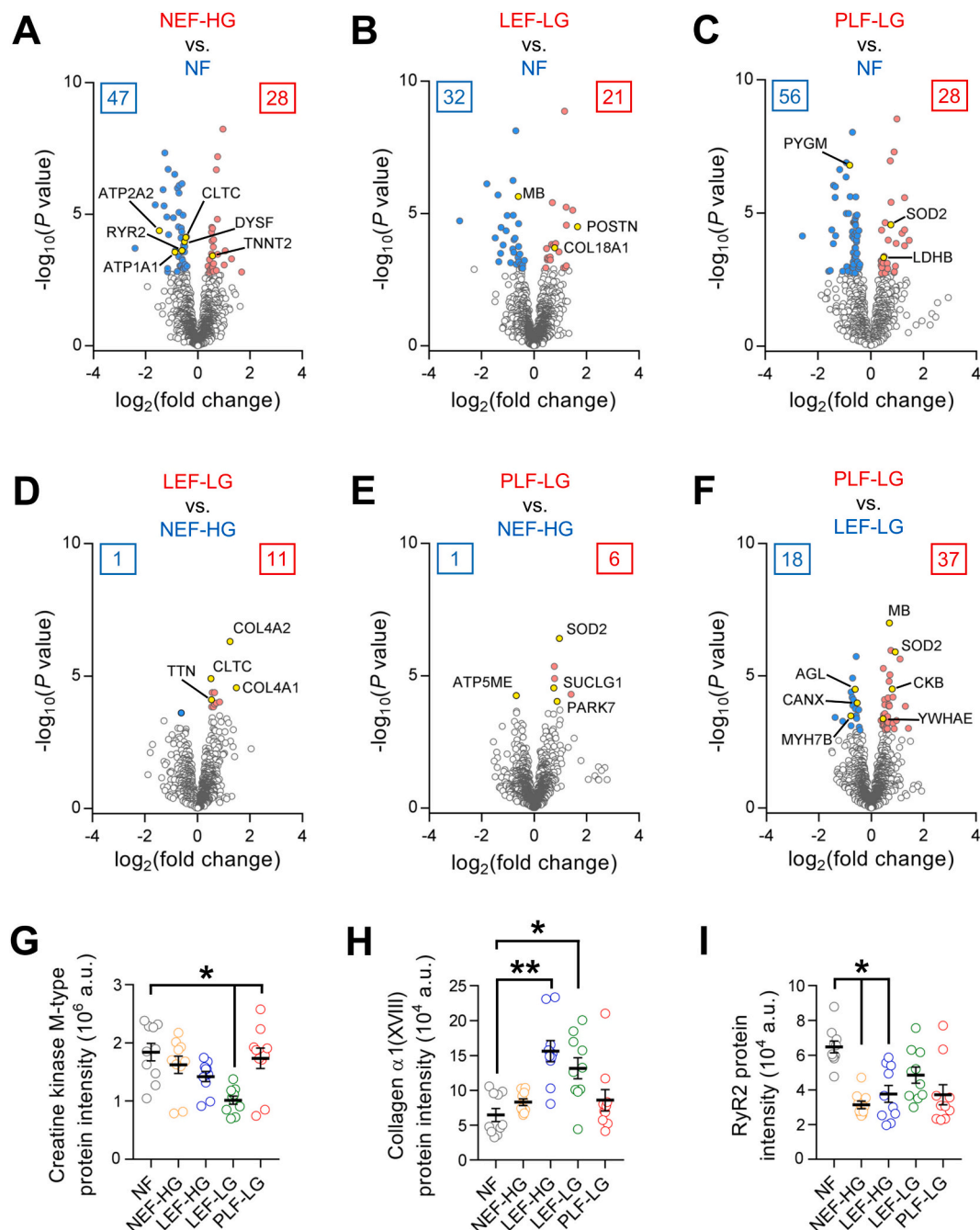
Fig. 3. Subtype-specific protein expression in AS left-ventricular biopsies. (A-C) Volcano plots showing the -$\log_{10}$ P values versus $\log_2$ fold changes for the AS proteotypes NEF-HG, LEF-HG, and PLF-LG compared to non-failing (NF) samples, and (D-F) pairwise comparisons of AS proteotypes NEF-HG, LEF-HG, and PLF-LG. The number of significantly up- or downregulated proteins is indicated on top, and up- or down-regulated proteins are indicated by red or blue colored dots, respectively (ANOVA, FDR < 0.05). Proteins of interest with essential cardiac functions are additionally highlighted in yellow and identified by gene labels. (G-I) Dot plots summarizing differential abundance changes of three proteins of interest as quantified by their label-free DIA-MS intensity. RyR2, ryanodine receptor type 2/ Ca^{2+} release channel. n = 5 LV biopsies from different patients were independently analyzed per group including 2 replicate injections per sample. Differential protein expression was tested for using the R package limma, accounting for the technical replication. P values were adjusted for multiple testing using the Benjamini-Hochberg procedure. * P < 0.05; ** P < 0.01. (For interpretation of the references to color in this figure legend, the reader is referred to the web version of this article.)

specific histomorphologic changes were evidenced, namely a profound cardiomyocyte hypertrophy in NEF-HG and LEF-HG, as well as perinuclear lipofuscin aggregates in PLF-LG, and both correlated with AS peak flow velocity.

3.5. AS induces transverse-axial tubule (TAT) network remodeling

Ventricular cardiomyocytes express a regular network of invaginated endomembrane TAT-structures that allows to rapidly activate thousands of intracellular Ca^{2+} release units upon membrane depolarization based on precise spatial coupling, but undergoes substantial membrane remodeling processes in cardiac diseases [32–34]. However, the
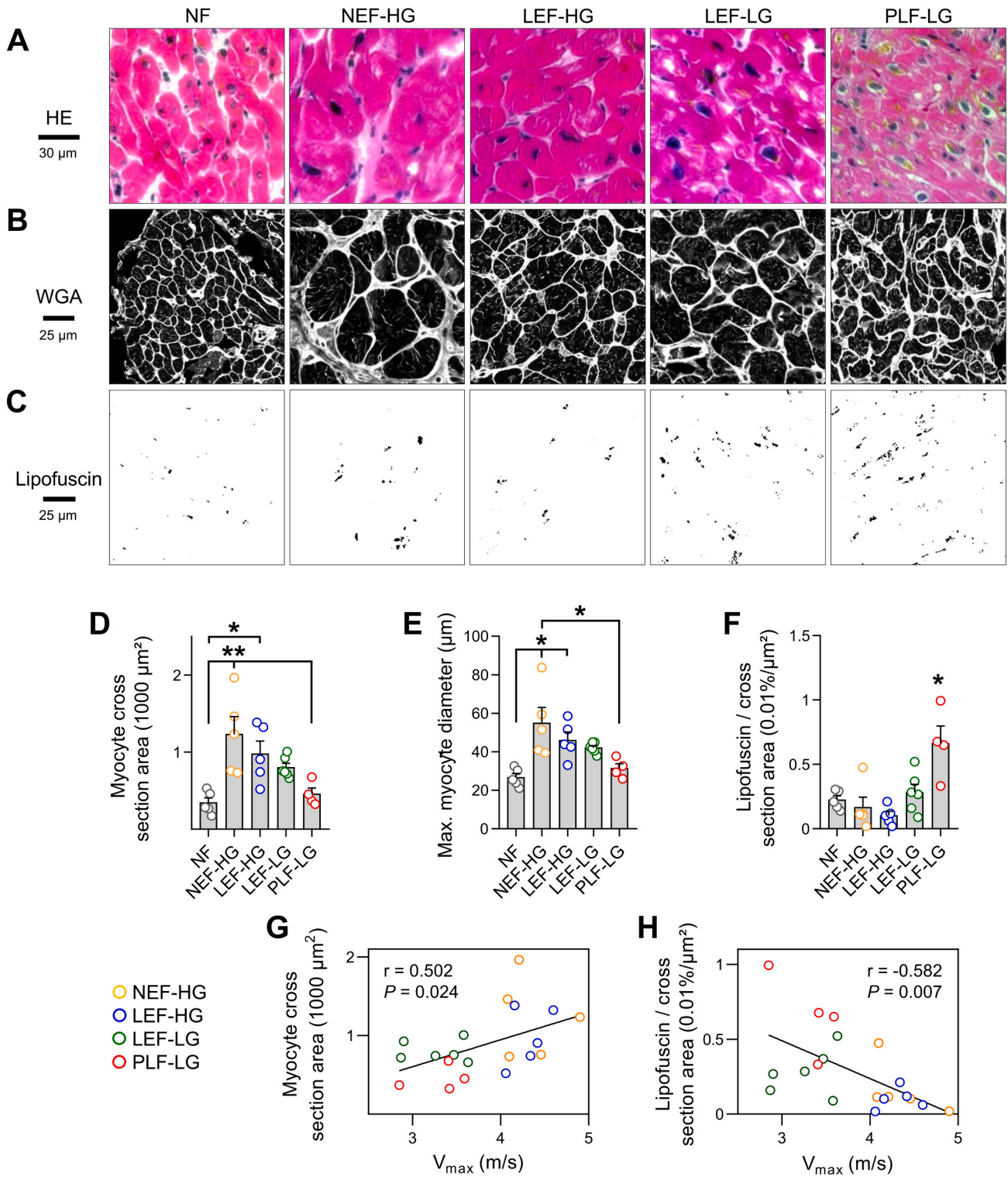
Fig. 4. Cardiomyocyte hypertrophy and lipofuscin aggregates manifest significantly, but differently between aortic stenosis subtypes. (A) Representative images of hematoxylin-eosin (HE) and (B) wheat germ agglutinin (WGA) stained histological cross-sections of LV myocardium. (A) Apparently, in transversally sectioned ventricular myocytes of human LV biopsies the degree of cardiomyocyte hypertrophy differs profoundly. Furthermore, excessive lipofuscin aggregates near the nuclei are most obvious in PLF-LG. (B) WGA stained sections confirming vastly different hypertrophy AS phenotypes based on cross-sectioned LV cardiomyocytes. (C) Representative image analysis depicting locally increased autofluorescence signals of lipofuscin aggregates in longitudinally sectioned cardiomyocytes. Dot plots and bar graphs summarizing the (D) mean cardiomyocyte cross-section area, (E) maximal cardiomyocyte diameter, and (F) lipofuscin aggregate area per myocyte cross section across different AS-subtypes compared to NF. * $P < 0.05$; ** $P < 0.01$, one-way ANOVA with post-hoc Tukey test. (G-H) Linear regression curves relating AS peak flow velocity (V_{max}) and cardiomyocyte hypertrophy (G), or lipofuscin deposition (H). r, *Pearson* correlation coefficient; *P*, *P* value. $n = 5/5/5/6/4$ independent patient LV biopsy sections.
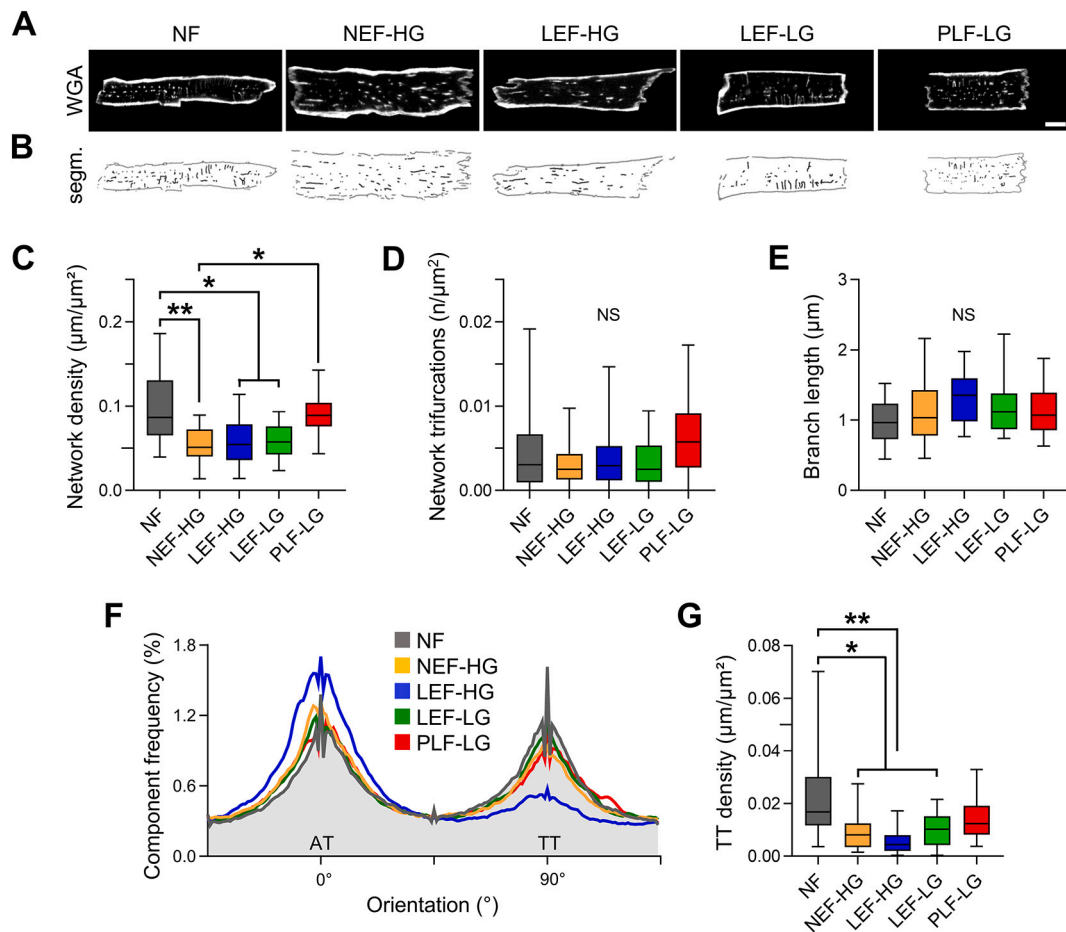
Fig. 5. Aortic stenosis causes subtype- and component-specific TAT network defects. (A) Confocal image panels of exemplary WGA-stained LV cardiomyocytes in tissue sections. Both intracellular TAT network components and the outer surface sarcolemma are visualized. (B) Digital image segmentation highlighting TAT component changes in the same cardiomyocytes shown in A. Scale 10 μm. Boxplots comparing (C) the mean TAT network density, (D) the number of network trifurcations, and (E) the branch length between AS-subtypes and NF control. (F) Histogram comparing the bimodal frequency distribution of the major TAT network components, specifically axial tubules (AT) at 0° and transverse tubules (TT) at 90°; binning ±0.5°. (G) Boxplot comparing the transverse tubule density (TT 90 ± 10°) between AS-subtypes and NF control. Boxplots indicate the median and the interquartile range, and whiskers represent the 5th and 95th percentiles. $n = 10$ LV myocytes each of 5/5/5/6/5 independent patient LV biopsy sections. * $P < 0.05$; ** $P < 0.01$, analyzed by linear mixed models with random intercepts for biological replicates and applying post-hoc Tukey's HSD tests.

organization of TAT-structures has never been analyzed between four different AS-subtypes. Here we used confocal imaging to visualize WGA labeled intracellular TAT-membrane structures inside cardiomyocytes in biopsy sections (Fig. 5A). The signal pattern in longitudinally oriented cardiomyocyte sections was analyzed by image segmentation to quantify specific TAT-network components as described previously (Fig. 5B) [35,36]. This showed a significantly decreased TAT-network density for NEF-HG, LEF-HG and LEF-LG compared to NF, but also a decreased TAT-network density for NEF-HG compared to PLF-LG (Fig. 5C). The density of TAT network trifurcations and the mean length of tubule segments were not significantly changed between AS-subtypes and NF due to high biological variances (Fig. 5D-E). Finally, while the frequency of major TAT-network components, namely axial (AT) and transverse (TT) tubules, was balanced in favor of TT in NF cardiomyocytes as expected (Fig. 5F, *grey*) [37], all AS-subtypes showed increased AT at the cost of TT components (Fig. 5F, *color legend*). Despite qualitatively similar changes, extreme TAT-network changes occurred in LEF-HG cardiomyocytes through a pronounced TT loss (Fig. 5F, *blue*). A significant decrease in the density of TT membrane components was found in NEF-HG, LEF-HG, and LEF-LG compared to NF, while TT-components seemed preserved in PLF-LG (Fig. 5G). Taken together, a decreased TAT-network density in NEF-HG, LEF-HG and LEF-LG and a loss of physiologically important TT-components supports subcellular disruption of EC

coupling in three out of four AS-subtypes.

3.6. RyR2-cluster fragmentation in AS with systolic heart failure

Based on the DIA-MS and TAT-network data, we hypothesized that a decreased RyR2 abundance (Fig. 3I) and a significant loss of TAT-network structures in different AS-subtypes (Fig. 5) may directly compromise the RyR2 channel cluster organization in AS. While confocal imaging of immunolabeled RyR2-clusters in NF cardiomyocytes confirmed the expected regular physiological distribution in transverse striations, AS-affected cardiomyocytes showed subcellular changes, disrupting the regular RyR2 distribution near *Z*-lines (Supplementary Fig. 11A). Accordingly, a decreased power in fast *Fourier* transformation of RyR2 imaging data confirmed a decreased striation of RyR2 signals (Supplementary Fig. 11B). To analyze the relation between RyR2-clustering and TAT-component changes at nanometric resolution, we used dual-color STED imaging of caveolin-3 (CAV3) and RyR2. While CAV3-positive AT and TT-components were frequently associated with RyR2-clusters in NF cardiomyocytes, AS-affected cardiomyocytes showed highly variable changes (Fig. 6A, *top*). Since RyR2-protein expression was variably decreased across AS-subtypes (Fig. 3I), subcellular RyR2-cluster changes were visualized by high-contrast image segmentation (please see the Supplementary Information) [21].
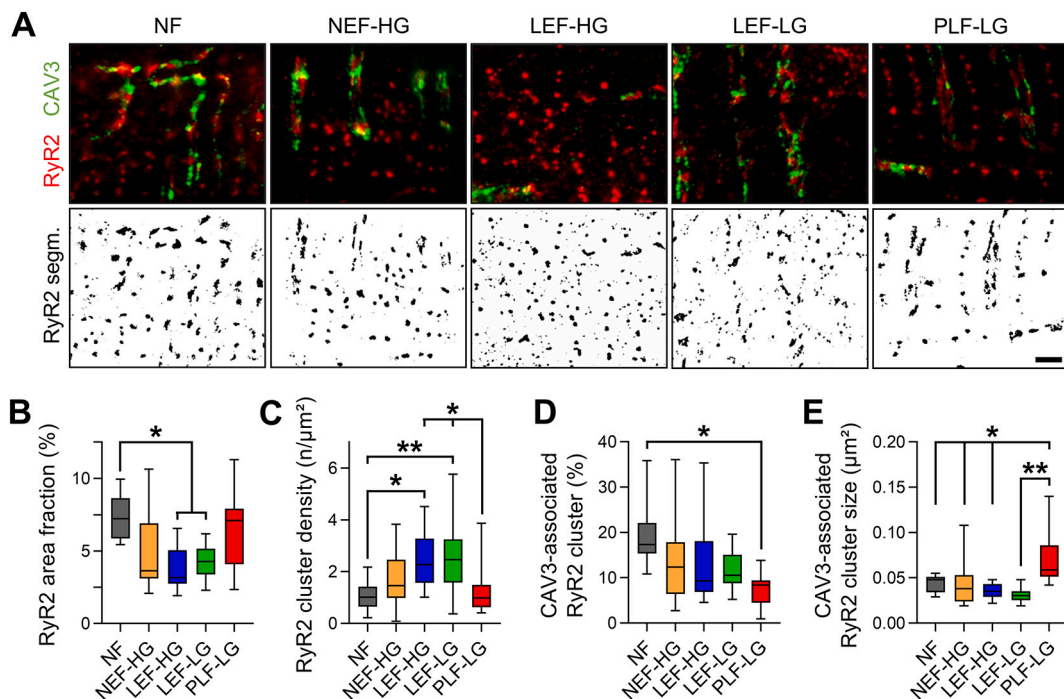
Fig. 6. Subcellular remodeling of RyR2-clustering and junctional coupling. (A) *Top:* Dual-color STED immunofluorescence images depicting magnified regions of interest inside longitudinally sectioned LV myocytes in biopsy tissue. Regions of interest were selected to represent RyR2 channel clusters (RyR2, *red*) organized in striations and associated junctional TAT components identified by caveolin-3 cluster signals (CAV3, *green*). *Bottom:* Image segmentation highlighting subcellular differences in RyR2-cluster signal distributions. Scale 1 μm. Boxplots comparing (B) the RyR2 area fraction, (C) the RyR2-cluster density, (D) the intracellular CAV3-associated RyR2-cluster fraction, and (E) the CAV3-associated RyR2-cluster size. Boxplots indicate the median and the interquartile range, and whiskers represent the 5th and 95th percentiles. $n = 5$ in B–C and $n = 3$ in D-E LV myocytes each of 5/5/5/6/5 independent patient LV biopsy sections. * $P < 0.05$; ** $P < 0.01$, analyzed by linear mixed models with random intercepts for biological replicates and applying post-hoc Tukey's HSD tests. (For interpretation of the references to color in this figure legend, the reader is referred to the web version of this article.)
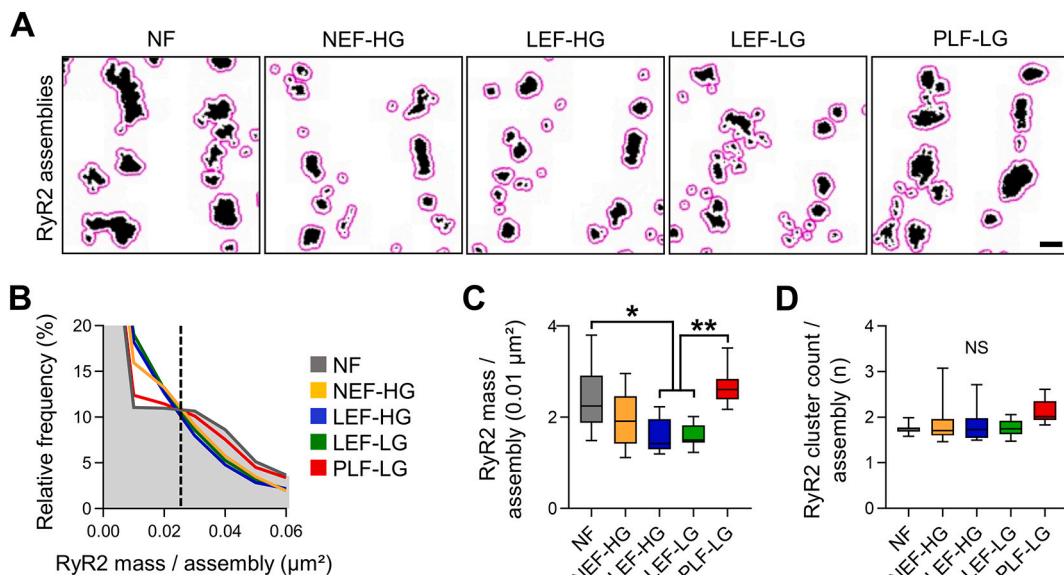

Fig. 7. RyR2-cluster fragmentation may contribute to the loss of locally assembled channel mass. (A) RyR2-clusters with a nearest-neighbor distance ≤100 nm are classified as functionally associated inter-cluster channel assemblies (*magenta boundaries*) by image analysis. Scale 250 nm. (B) Histogram showing the relative frequency distribution of the RyR2 signal mass per inter-cluster assembly; binning ±0.005 μm². The dashed vertical line indicates decreased RyR2 mass per inter-cluster assembly for NEF-HG, LEF-HG, and LEF-LG (*left side*) versus higher RyR2 mass per inter-cluster assembly for NF control and PLF-LG (*right*). Boxplots comparing (C) the RyR2 signal mass, and (D) the RyR2-cluster count per assembly. Boxplots indicate the median and the interquartile range, and whiskers represent the 5th and 95th percentiles. $n = 3$ LV myocytes each of 5/5/5/6/5 independent patient LV biopsy sections. * $P < 0.05$; *** $P < 0.001$, analyzed by linear mixed models with random intercepts for biological replicates and applying post-hoc Tukey's HSD tests. (For interpretation of the references to color in this figure legend, the reader is referred to the web version of this article.)

Apparently, the striation-associated RyR2-cluster pattern was strongly diminished in LEF-HG and LEF-LG cardiomyocyte sections (Fig. 6A, *bottom*).

Image analysis confirmed a significantly decreased RyR2 area fraction in LEF-HG and LEF-LG compared to NF (Fig. 6B). Despite a decreased area fraction, the subcellular RyR2-cluster density was increased in LEF-HG and LEF-LG compared to NF and PLF-LG (Fig. 6C). Together, these findings indicate a RyR2-cluster fragmentation process, potentially contributing to depressed LVEF in two AS-subtypes. However, a decreased RyR2-cluster association with CAV3-positive TT-components occurred only in PLF-LG (Fig. 6D), where significantly larger transversal RyR2-cluster plaques were evidenced (Fig. 6E). In sharp contrast, LEF-HG and LEF-LG cardiomyocytes showed significantly smaller CAV3-associated RyR2-clusters (Fig. 6E). Hence, super-resolution image analysis extended our finding of decreased RyR2-protein levels to subcellular RyR2-cluster fragmentation in LEF-HG and LEF-LG. Moreover, whereas CAV3-associated RyR2-clustering was decreased in PLF-LG, a preserved TAT-network associated with enlarged RyR2-cluster plaques may sustain EC coupling.

3.7. RyR2-cluster fragmentation disrupts Ca^{2+} release units in AS

In rat cardiomyocytes, one third of RyR2-clusters exist within ≤100 nm neighbor-to-neighbor distance and can thus functionally interact in Ca^{2+} release units [38]. However, in human cardiomyocytes from AS patients lateral distances between RyR2-clusters are currently unknown. We confirmed that neighboring RyR2-clusters frequently occur as assemblies with ≤100 nm inter-cluster spacing in NF cardiomyocytes, but also in PLF-LG (Fig. 7A, *magenta boundaries*). In three AS-subtypes, NEF-HG, LEF-HG and LEF-LG, the observed RyR2-cluster fragmentation led

to smaller inter-cluster assemblies (Fig. 7A). Statistical analysis confirmed a reduction of RyR2 assembly signal mass in LEF-HG and LEF-LG (Fig. 7B-C). The RyR2-cluster count per inter-cluster assembly was not changed between AS-subtypes and NF (Fig. 7D). Thus, from the perspective of Ca^{2+} release units, RyR2-cluster fragmentation in LEF-HG and LEF-LG may additionally diminish RyR2 channel numbers within functional inter-cluster assemblies, leading to a reduced local systolic Ca^{2+} release flux.

3.8. RyR2-cluster fragmentation correlates with left-ventricular dysfunction

To investigate the relation between RyR2-cluster fragmentation and left-ventricular dysfunction independent of any a priori AS-subtype classification, we applied univariate linear regression modeling using the simulation extrapolation (SIMEX) algorithm and 1000 iterations [24,25]. Specifically, for echocardiographic data the interventricular septum (IVS) thickness, the LVEDD, and the LVEF were correlated with histomorphologic, TAT-network and nanometric RyR2-cluster changes in cardiomyocytes in situ (Table 1).

As expected, 75.6% of all AS patients developed an IVS thickness > 13 mm consistent with septal hypertrophy. Surprisingly, cardiomyocyte cross-section area and maximal diameter did not reach statistical significance to prove a correlation with septal hypertrophy (Table 1A). However, the lipofuscin area fraction and LVEDD were inversely correlated, whereas the cross-section normalized lipofuscin area and LVEF were positively correlated (Table 1A). Interestingly, a significant increase in TAT-network trifurcations was positively correlated with septal hypertrophy (Table 1B). We confirmed that this correlation remains valid for PLF-LG, where cardiomyocyte cross-section area and

Table 1

Univariate linear regression modeling correlating cardiomyocyte morphology and subcellular changes with echocardiographic left-ventricular structure and function. In order to consider multiple measurements of independent variables, we applied a simulation extrapolation (SIMEX) algorithm using 1000 iterations [24,25]. Co-efficient represents the regression coefficient. *P* values < 0.05 are indicated in bold. IVS, interventricular septum; LVEDD, left-ventricular end-diastolic diameter; LVEF, left-ventricular ejection fraction; SE, standard error; SD, standard deviation.

Parameter	Count (n)	Mean ± SD	IVS (mm)			LVEDD (mm)			LVEF (%)		
			Coefficient	SE	*P* value	Coefficient	SE	*P* value	Coefficient	SE	*P* value
A) LV myocyte histomorphology											
Myocyte cross section area (μm²)	21	775 ± 431	−0.002	0.001	0.236	0.001	0.005	0.857	−0.007	0.009	0.452
Max. myocyte diameter (μm)	21	41 ± 13	−0.051	0.044	0.269	−0.016	0.157	0.919	−0.143	0.296	0.635
Lipofuscin area fraction (%)	21	1.7 ± 1.1	0.383	0.511	0.463	−4.096	1.490	**0.013**	5.895	3.054	0.069
Lipofuscin / cross section area (%/μm²)	21	0.0027 ± 0.0024	361.4	207.0	0.098	−1378	694.4	0.062	3104	1251	**0.023**
B) TAT network organization											
TAT density (μm/μm²)	210	0.07 ± 0.024	54.14	27.05	0.059	−87.83	100.2	0.392	317.8	182.7	0.098
TAT trifurcations (n/μm²)	210	0.0043 ± 0.0024	641.8	246.3	**0.017**	−179.1	992.1	0.859	2148	1883	0.268
C) RyR2 cluster analysis											
RyR2 area fraction (%)	105	5.2 ± 2	0.217	0.327	0.515	0.025	1.087	0.982	3.369	2.030	0.113
RyR2 cluster density (n/μm²)	105	1.8 ± 0.86	−1.436	0.686	**0.049**	3.063	2.539	0.242	−11.89	4.405	**0.014**
Large RyR2 cluster density (n/μm²)	105	0.0061 ± 0.0055	167.4	161.6	0.313	−79.27	520.2	0.881	2147	913.0	**0.029**
Small RyR2 cluster density (n/μm²)	105	1.4 ± 0.74	−1.569	0.789	0.062	3.289	2.910	0.273	−14.01	4.979	**0.011**
CAV3-associated RyR2 clusters (%)	63	13 ± 6.8	−0.030	0.092	0.746	−0.296	0.311	0.354	0.223	0.609	0.718
RyR2 cluster size CAV3-associated (μm²)	63	0.044 ± 0.019	31.94	29.35	0.290	−111.4	105.6	0.305	488.0	199.4	**0.024**
RyR2 cluster size not CAV3-associated (μm²)	63	0.013 ± 0.0039	195.7	212.5	0.369	−526.0	722.6	0.476	3309	1282	**0.018**
D) Functional RyR2 cluster analysis											
RyR2 assembly area (μm²)	63	0.06 ± 0.012	50.74	47.85	0.302	−88.99	164.3	0.594	823.7	274.9	**0.007**
RyR2 mass / assembly (μm²)	63	0.019 ± 0.0053	127.1	111.3	0.268	−260.9	381.6	0.502	2073	626.3	**0.004**
RyR2 area fraction / assembly (%)	63	21 ± 1.9	0.538	0.319	0.108	−0.352	1.113	0.755	4.762	1.962	**0.025**
RyR2 cluster size / assembly (μm²)	63	0.011 ± 0.002	401.5	301.1	0.198	−908.5	1034	0.391	5644	1707	**0.004**
RyR2 cluster count / assembly (n)	63	1.9 ± 0.36	0.577	1.586	0.719	−1.428	5.392	0.794	16.23	10.06	0.123
RyR2 cluster density / assembly (n/μm²)	63	51 ± 4	−0.222	0.158	0.176	−0.252	0.549	0.652	−0.736	1.071	0.500
RyR2 cluster size / assembly (μm²)	63	0.011 ± 0.002	401.5	301.1	0.198	−908.5	1034	0.391	5644	1707	**0.004**

maximal diameter were not significantly changed (Fig. 4D-E).

Importantly, we identified significant correlations between RyR2-cluster changes and left-ventricular function (Table 1C). Particularly, the spatial density of large RyR2-clusters (0.101–0.12 μm²), both CAV3-associated *or* not, positively correlated with LVEF (Table 1C). Strikingly, the density of small RyR2-clusters (≤ 0.02 μm²) showed an inverse correlation with systolic left-ventricular function (Table 1C). This suggests that left-ventricular dysfunction in AS is associated with RyR2-cluster fragmentation.

Finally, RyR2 inter-cluster assemblies, defined by a nearest-neighbor-distance ≤100 nm, and LVEF were correlated, further supporting correlations with left-ventricular function (Table 1D). Additionally, the RyR2 assembly area, as well as RyR2 mass, area, and cluster size per inter-cluster assembly were strongly correlated with LVEF (Table 1D). Taken together, univariate regression modeling identified significant correlations between preserved systolic left-ventricular function and the presence of both larger RyR2-clusters and inter-cluster assemblies. Vice versa, increased RyR2-cluster fragmentation was significantly correlated with left-ventricular loss-of-function and heart failure in patients.

4. Discussion

In severe AS, myocardial function and left-ventricular fate differ profoundly between patients for previously unknown reasons. To explore the cellular and molecular disease mechanisms in an unbiased fashion, we established a state-of-the-art quantitative DIA-MS workflow to analyze individual small left-ventricular biopsies proteome-wide. Based on a reproducible coverage of 2273 proteins between all biopsy samples, we investigated the hypothesis that unique ventricular AS proteotypes exist that segregate differentially and, thus, can directly identify distinct myocardial AS phenotypes. Indeed, unbiased hierarchical clustering and proteomic profiling suggested three unique AS proteotypes for the first time. Furthermore, superresolution imaging informed and directed by proteomic expression profiling confirmed distinct subcellular changes, for example a decrease of RyR2 protein expression and RyR2 channel clustering likely to directly affect subcellular Ca²⁺ release in cardiomyocytes, as these changes were positively correlated with left-ventricular systolic dysfunction.

In individual left-ventricular biopsies, we reliably detected and quantified not only 2273 proteins, of which 160 showed differential abundance changes, but provided the first proteomic profiling that investigates proteotypes among previously echocardiographically defined AS-subtypes. Specifically, hierarchical clustering segregated a unique proteotype for each of three clinically established hemodynamic AS-subtypes: NEF-HG, LEF-LG and PLF-LG. In contrast, LEF-HG clustered in two separate proteotype subgroups, either LVEF > 30% or ≤ 30%, where the former was closely associated with the NEF-HG and the latter with the LEF-LG proteomic changes.

Histomorphology confirmed and extended the proteomic findings. Strikingly, contrasting with prevailing models of an AS-induced severe hypertrophy phenotype, left-ventricular cardiomyocyte size differs substantially between AS-subtypes, ranked in the order NF < PLF-LG < LEF-LG < LEF-HG < NEF-HG. This indicates, particularly between the extremes of PLF-LG with minimal left-ventricular cardiomyocyte enlargement versus NEF-HG with a very prominent cardiomyocyte size increase, that distinctive hypertrophy states may exist that further correlate with echocardiographic AS peak flow velocity.

In line with distinct AS-induced cardiomyocyte cellular fates, the subcellular TAT endomembrane network and RyR2-cluster organization were also differentially affected between different AS-subtypes. While a reduced TAT-network density in NEF-HG, LEF-HG and LEF-LG was evident, supporting a functional disruption through EC *un*-coupling, strikingly a substantial RyR2-cluster fragmentation process has been visualized and quantified only in those AS-subtypes with a significantly depressed left-ventricular function. Finally, univariate regression

modeling confirmed the positive correlation between RyR2-cluster fragmentation and decreased left-ventricular contractility, implicating causative cellular and molecular defects for the left-ventricular loss-of-function of the LEF-HG and LEF-LG subtypes.

4.1. Proteomic approaches differentiate distinct AS-subtypes

25-to-35% of patients with severe AS and preserved LVEF are diagnosed with transvalvular PLF-LG [39]. In 15% of all patients undergoing surgical open-chest AVR, LVEF is depressed, here represented by patients with LEF-HG and LEF-LG [40]. Since mortality following AVR is increased in all these three AS-subtypes as compared to the 'classic' NEF-HG, improved mechanistic understanding is important to dissect the molecular differences and potential biomarkers that can identify unique AS-subtypes.

Indeed, hierarchical clustering established distinctive proteotypes each for NEF-HG, LEF-LG and PLF-LG, thereby principally supporting the echocardiography-based stratification in severe AS as recommended in current clinical guidelines [1,2]. However, LEF-HG clustered either with NEF-HG or LEF-LG (Fig. 1B-C), while histomorphology (Fig. 4) and STED imaging (Figs. 6 and 7) confirmed intermediate hypertrophy and RyR2-cluster fragmentation states. Hence, the LEF-HG biopsies may indicate transitory states between milder hypertrophy and systolic heart failure. Interestingly, hierarchical clustering placed LEF-LG and NF next to each other, whereas NEF-HG showed the greatest Euclidean distance from NF (Fig. 1C). This may indicate that the proteome-wide changes involved in hypertrophic remodeling exceed those of contractile failure in LEF-LG. Finally, there was a non-significant trend for cardiomyocyte hypertrophy, while lipofuscin aggregates were highly abundant in PLF-LG (Fig. 4F), further confirming unique proteotype-phenotype relations.

4.2. TAT-network changes contributing to left-ventricular dysfunction

Electron microscopy showed TT changes in biopsies from hypertrophied hearts including AS previously [41]. A pathophysiological reorganization of the TAT-network is widely accepted as mechanism directly contributing to contractile dysfunction in different disease models [42]. Crossman et al. recently showed that TT reorganization correlates regionally with contractile dysfunction in human hearts [32]. Furthermore, Seidel et al. reported TAT-network changes impairing functional recovery following mechanical unloading in end-stage heart failure [43]. Consistent with these reports, analysis of left-ventricular cardiomyocytes in biopsy sections revealed a significantly decreased TAT-network density in LEF-HG and LEF-LG (Fig. 5C). Albeit to different degrees, all AS-subtypes exhibited increased AT-components at the cost of TT-components (Fig. 5F), previously termed 'axialization' [44].

4.3. RyR2-cluster fragmentation and systolic dysfunction

Functionally relevant RyR2-clustering occurs in junctional Ca²⁺ release units [38,45–47]. Due to decreases in TT-structures and TAT-network density (Fig. 5), junctional RyR2-cluster activation appears disrupted to different degrees across AS-subtypes (Fig. 6). Confocal imaging identified a small decrease in RyR2-cluster density in human dilated cardiomyopathy previously [48]. Here, STED imaging revealed the complexity of RyR2-cluster changes, demonstrating RyR2-cluster fragmentation for the first time in LEF-HG and LEF-LG for AS-subtypes with a depressed LVEF (Fig. 6C). In contrast, RyR2-clustering occurred in unusually large transversal plaques, while LVEF was preserved in PLF-LG (Fig. 6E). Though we note that the RyR2 area fraction and cluster density were not changed in NEF-HG (Fig. 6B and C), a decreased RyR2 abundance as shown by DIA-MS (Fig. 3I) supports a functionally relevant dispersion of smaller RyR2 clusters that may impair subcellular Ca²⁺ release.

For RyR2 inter-cluster analysis (Fig. 7), a distance of ≤100 nm was used in accordance with Baddeley et al. [38]. In a sheep model with

persistent atrial fibrillation, Macquaide et al. observed atrial RyR2-cluster fragmentation and an increased Ca^{2+} spark frequency, where Ca^{2+} release units were defined by <150 nm inter-cluster distances [49]. While left-ventricular biopsies are not amenable for live-cell Ca^{2+} imaging, univariate regression modeling confirmed a significant correlation between increased RyR2-cluster fragmentation and depressed left-ventricular systolic function (Table 1). Follow-up studies will need to confirm RyR2-cluster fragmentation by electron microscopy, and clarify the role of RyR2 cluster disorganization for life-threatening arrhythmias as potential causes of increased mortality in AS patients.

4.4. Implications for the treatment of AS patients

Proteome analysis by DIA-MS and hierarchical clustering identified left-ventricular protein profiles that differentiate three unique proteotypes each for NEF-HG, LEF-LG, and PLF-LG. These differentially abundant proteins include essential proteins with major roles in cardiac physiology and disease (Fig. 3). Interestingly, Peterzan et al. identified creatine kinase capacity and/or flux as a therapeutic strategy for systolic heart failure in AS [50], consistent with our finding of significantly reduced *CKM* in LEF-LG (Fig. 3G). Notably, the echocardiography parameters LVEF and LVEDD correlated significantly with protein abundance changes, underlining the potential of proteomic approaches for future development of diagnostic and therapeutic biomarkers.

The exploratory design of this study allowed applying state-of-the-art MS and superresolution imaging techniques on a limited number of small transcatheter LV biopsies to identify key biological processes in severe AS. These methods revealed significant proteomic and subcellular changes that may lead to establish subtype-specific biomarkers for prediction of individual patient outcomes in symptomatic (severe) AS. In addition, the proteomic findings may open avenues for mechanistic analysis in animal and stem cell models towards pharmacological targeting of specific AS-subtypes. Furthermore, replication studies with higher numbers of patient samples are needed to verify our findings, and to fully establish biopsy-guided diagnostic biomarkers that extend the current echocardiography-based risk stratification in AS to cellular and molecular mechanisms. Although we are careful to note that LV biopsies are associated with severe complications, these were quantified to less than < 1% in experienced hands [51]. Hence, we agree with Frey et al. that novel biopsy-guided diagnostic strategies including proteomic profiling and superresolution imaging may have an important impact on the personalized treatment of complex forms of heart disease such as AS [52]. Although all patients included in this study suffered from severe AS leading to pressure-overload of the left ventricle, three AS proteotypes were described prioritizing different molecular and subcellular remodeling mechanisms that may be addressed specifically in future clinical practice.

4.5. Study limitations

This study allowed for the proteomic and microscopic analysis of small precious LV biopsies directly comparing four hemodynamic subtypes of severe AS. While the subtype size of $n = 5$ LV biopsies per group for proteomic analysis is relatively small, a large number of over > 2000 proteins were routinely identified throughout all samples. An additional limitation has been access to LV biopsies from patients with severe AS for corresponding proteomic *and* microscopic analyses. Here, only three patients are represented across all analyses. Hence, LEF-HG biopsies could not be assigned to the proteotypes NEF-HG, LEF-LG and PLF-LG in microscopic analyses. Furthermore, to allow for sufficient biopsy numbers throughout all four AS-subtypes, patients with CAD, AF and other comorbidities needed to be included. A 66% prevalence of CAD suggests that the observed proteomic changes are at least partially subject to these confounding factors (Supplementary Tables 1–3). However, when comparing patients with and without CAD, or patients with and without AF, respectively, no protein at all remained

significantly regulated between these groups after adjusting for multiple testing (Supplementary Fig. 7), in sharp contrast to the pairwise AS-subtype comparisons with multiple differentially regulated proteins (Fig. 3). Nevertheless, by inclusion of frequently observed comorbidities like CAD and AF, our patient cohort is representative for the TAVR population at large. This pioneer study may help to stimulate and legitimate replication studies with higher numbers of left-ventricular biopsies to verify and extend our molecular and subcellular findings in AS.

4.6. Conclusions

We demonstrate for the first time the in-depth quantitative proteomic profiling of individual small left-ventricular biopsy samples in an exploratory patient trial of severe AS-subtype fates. Hierarchical clustering identified 160 differential protein abundance changes and three segregated AS-subtypes each with unique proteotypes. These AS-subtypes, namely NEF-HG, LEF-LG, and PLF-LG, each showed significant correlations between their specific protein and echocardiographic changes. Interestingly, histomorphology confirmed and extended previously unknown AS-subtype specific differences in the extent of left-ventricular cardiomyocyte hypertrophy and local perinuclear lipofuscin aggregation. Informed by the unbiased proteomic expression profiling and based on a variably, as well as significantly decreased subtype-specific RyR2 protein abundance, superresolution imaging of immunostained tissue sections showed different degrees of disorganization of Ca^{2+} release units between different AS-subtypes. Together with a significantly decreased TAT-network density, RyR2-cluster fragmentation in human cardiomyocytes was most pronounced in LEF-HG and LEF-LG, supporting a new disease mechanism of EC *un*-coupling specifically in AS patients with left-ventricular systolic dysfunction. Furthermore, univariate regression modeling confirmed that RyR2-cluster fragmentation significantly correlates with systolic loss-of-function. In summary, quantitative DIA-MS analysis of myocardial biopsies not only defines the proteome-wide nature of and molecular differences between unique AS-subtypes, but opens avenues for a subtype-specific biomarker screening based on extracellular and intracellular proteotype changes, as well as mechanistic studies of the here reported AS-subtype specific contractile dysfunction and the potential for therapeutic recovery towards precision medicine.

Data availability

Mass spectrometry proteomic data have been deposited to the ProteomeXchange Consortium via the PRIDE [53] partner repository with the dataset identifier PXD019594. All other data supporting the findings

of this study are available upon reasonable request.

Authors' contributions

CL, GH, SB and SEL contributed to the study conception and design. Material preparation, data collection and analysis were performed by AL, BEB, CFJ, CJ, CL, FK, HLS, IK, KT, LD, LN, MP, NJP, RT, SB, TK and TS. The first draft of the manuscript was written by SB and SEL, and all authors commented on previous versions of the manuscript. All authors read and approved the final manuscript.

Declaration of Competing Interest

SEL is an inventor on patent (US 20070089572A1) submitted by Columbia University "Novel agents for preventing and treating disorders involving modulation of RYR receptors".

Appendix A. Supplementary data

Supplementary data to this article can be found online at https://doi.org/10.1016/j.yjmcc.2022.08.363.

References

[1] C.M. Otto, R.A. Nishimura, R.O. Bonow, B.A. Carabello, J.P. Erwin 3rd, F. Gentile, H. Jneid, E.V. Krieger, M. Mack, C. McLeod, P.T. O'Gara, V.H. Rigolin, T. M. Sundt 3rd, A. Thompson, C. Toly, 2020 ACC/AHA guideline for the management of patients with valvular heart disease: a report of the American College of Cardiology/American Heart Association Joint Committee on Clinical Practice Guidelines, Circulation 143 (5) (2021) e72–e227.

[2] A. Vahanian, F. Beyersdorf, F. Praz, M. Milojevic, S. Baldus, J. Bauersachs, D. Capodanno, L. Conradi, M. De Bonis, R. De Paulis, V. Delgado, N. Freemantle, M. Gilard, K.H. Haugaa, A. Jeppsson, P. Juni, L. Pierard, B.D. Prendergast, J. R. Sadaba, C. Tribouilloy, W. Wojakowski, E.E.S.D. Group, 2021 ESC/EACTS Guidelines for the management of valvular heart disease, Eur. Heart J. 43 (7) (2022) 561–632.

[3] B. Iung, G. Baron, E.G. Butchart, F. Delahaye, C. Gohlke-Barwolf, O.W. Levang, P. Tornos, J.L. Vanoverschelde, F. Vermeer, E. Boersma, P. Ravaud, A. Vahanian, A prospective survey of patients with valvular heart disease in Europe: the euro heart survey on valvular heart disease, Eur. Heart J. 24 (13) (2003) 1231–1243.

[4] V.T. Nkomo, J.M. Gardin, T.N. Skelton, J.S. Gottdiener, C.G. Scott, M. Enriquez-Sarano, Burden of valvular heart diseases: a population-based study, Lancet 368 (9540) (2006) 1005–1011.

[5] C.M. Otto, B.K. Lind, D.W. Kitzman, B.J. Gersh, D.S. Siscovick, Association of aortic-valve sclerosis with cardiovascular mortality and morbidity in the elderly, N. Engl. J. Med. 341 (3) (1999) 142–147.

[6] C.M. Otto, Calcific aortic stenosis–time to look more closely at the valve, N. Engl. J. Med. 359 (13) (2008) 1395–1398.

[7] K. Al-Azizi, M. Hamandi, M. Mack, Clinical trials of transcatheter aortic valve replacement, Heart 105 (Suppl. 2) (2019) s6–s9.

[8] M.B. Leon, C.R. Smith, M. Mack, D.C. Miller, J.W. Moses, L.G. Svensson, E. M. Tuzcu, J.G. Webb, G.P. Fontana, R.R. Makkar, D.L. Brown, P.C. Block, R. A. Guyton, A.D. Pichard, J.E. Bavaria, H.C. Herrmann, P.S. Douglas, J.L. Petersen, J.J. Akin, W.N. Anderson, D. Wang, S. Pocock, P.T. Investigators, Transcatheter aortic-valve implantation for aortic stenosis in patients who cannot undergo surgery, N. Engl. J. Med. 363 (17) (2010) 1597–1607.

[9] H.P. Krayenbuehl, O.M. Hess, E.S. Monrad, J. Schneider, G. Mall, M. Turina, Left ventricular myocardial structure in aortic valve disease before, intermediate, and late after aortic valve replacement, Circulation 79 (4) (1989) 744–755.

[10] S. Hein, E. Arnon, S. Kostin, M. Schonburg, A. Elsasser, V. Polyakova, E.P. Bauer, W.P. Klovekorn, J. Schaper, Progression from compensated hypertrophy to failure in the pressure-overloaded human heart: structural deterioration and compensatory mechanisms, Circulation 107 (7) (2003) 984–991.

[11] S. Doll, M. Dressen, P.E. Geyer, D.N. Itzhak, C. Braun, S.A. Doppler, F. Meier, M. A. Deutsch, H. Lahm, R. Lange, M. Krane, M. Mann, Region and cell-type resolved quantitative proteomic map of the human heart, Nat. Commun. 8 (1) (2017) 1469.

[12] C.J. Coats, W.E. Heywood, A. Virasami, N. Ashrafi, P. Syrris, C. Dos Remedios, T. A. Treibel, J.C. Moon, L.R. Lopes, C.G.A. McGregor, M. Ashworth, N.J. Sebire, W.

J. McKenna, K. Mills, P.M. Elliott, Proteomic analysis of the myocardium in hypertrophic obstructive cardiomyopathy, Circ. Genom. Precis. Med. 11 (12) (2018), e001974.

[13] J. Lim, J.T. Aguilan, R.S. Sellers, F. Nagajyothi, L.M. Weiss, R.H. Angeletti, A. E. Bortnick, Lipid mass spectrometry imaging and proteomic analysis of severe aortic stenosis, J. Mol. Histol. 51 (5) (2020) 559–571.

[14] F. Schlotter, A. Halu, S. Goto, M.C. Blaser, S.C. Body, L.H. Lee, H. Higashi, D. M. DeLaughter, J.D. Hutcheson, P. Vyas, T. Pham, M.A. Rogers, A. Sharma, C. E. Seidman, J. Loscalzo, J.G. Seidman, M. Aikawa, S.A. Singh, E. Aikawa, Spatiotemporal multi-omics mapping generates a molecular atlas of the aortic valve and reveals networks driving disease, Circulation 138 (4) (2018) 377–393.

[15] T. Guo, P. Kouvonen, C.C. Koh, L.C. Gillet, W.E. Wolski, H.L. Rost, G. Rosenberger, B.C. Collins, L.C. Blum, S. Gillessen, M. Joerger, W. Jochum, R. Aebersold, Rapid mass spectrometric conversion of tissue biopsy samples into permanent quantitative digital proteome maps, Nat. Med. 21 (4) (2015) 407–413.

[16] L.S. Song, E.A. Sobie, S. McCulle, W.J. Lederer, C.W. Balke, H. Cheng, Orphaned ryanodine receptors in the failing heart, Proc. Natl. Acad. Sci. U. S. A. 103 (11) (2006) 4305–4310.

[17] A.M. Gomez, H.H. Valdivia, H. Cheng, M.R. Lederer, L.F. Santana, M.B. Cannell, S. A. McCune, R.A. Altschuld, W.J. Lederer, Defective excitation-contraction coupling in experimental cardiac hypertrophy and heart failure, Science 276 (5313) (1997) 800–806.

[18] H.B. Zhang, R.C. Li, M. Xu, S.M. Xu, Y.S. Lai, H.D. Wu, X.J. Xie, W. Gao, H. Ye, Y. Y. Zhang, X. Meng, S.Q. Wang, Ultrastructural uncoupling between T-tubules and sarcoplasmic reticulum in human heart failure, Cardiovasc. Res. 98 (2) (2013) 269–276.

[19] R.M. Lang, L.P. Badano, V. Mor-Avi, J. Afilalo, A. Armstrong, L. Ernande, F. A. Flachskampf, E. Foster, S.A. Goldstein, T. Kuznetsova, P. Lancellotti, D. Muraru, M.H. Picard, E.R. Rietzschel, L. Rudski, K.T. Spencer, W. Tsang, J.U. Voigt, Recommendations for cardiac chamber quantification by echocardiography in adults: an update from the American Society of Echocardiography and the European Association of Cardiovascular Imaging, J. Am. Soc. Echocardiogr. 28 (1) (2015) (1–39 e14).

[20] M. Puls, B.E. Beuthner, R. Topci, A. Vogelgesang, A. Bleckmann, M. Sitte, T. Lange, S.J. Backhaus, A. Schuster, T. Seidler, I. Kutschka, K. Toischer, E.M. Zeisberg, C. Jacobshagen, G. Hasenfuss, Impact of myocardial fibrosis on left ventricular remodelling, recovery, and outcome after transcatheter aortic valve implantation in different haemodynamic subtypes of severe aortic stenosis, Eur. Heart J. 41 (2020) 1903–1914.

[21] S. Brandenburg, J. Pawlowitz, B. Eikenbusch, J. Peper, T. Kohl, G.Y. Mitronova, S. Sossalla, G. Hasenfuss, X.H. Wehrens, P. Kohl, E.A. Rog-Zielinska, S.E. Lehnart, Junctophilin-2 expression rescues atrial dysfunction through polyadic junctional membrane complex biogenesis, JCI Insight 4 (12) (2019).

[22] K.M. Alsina, M. Hulsurkar, S. Brandenburg, D. Kownatzki-Danger, C. Lenz, H. Urlaub, I. Abu-Taha, M. Kamler, D.Y. Chiang, S.K. Lahiri, J.O. Reynolds, A. P. Quick, L. Scott Jr., T.A. Word, M.D. Gelves, A.J.R. Heck, N. Li, D. Dobrev, S. E. Lehnart, X.H.T. Wehrens, Loss of protein phosphatase 1 regulatory subunit PPP1R3A promotes atrial fibrillation, Circulation 140 (2019) 681–693.

[23] S. Brandenburg, J. Pawlowitz, V. Steckmeister, H. Subramanian, D. Uhlenkamp, M. Scardigli, M. Mushtaq, S.I. Amlaz, T. Kohl, J.W. Wegener, D.A. Arvanitis, D. Sanoudou, L. Sacconi, G. Hasenfuß, N. Voigt, V.O. Nikolaev, S.E. Lehnart, A junctional cAMP compartment regulates rapid Ca^{2+} signaling in atrial myocytes, J. Mol. Cell. Cardiol. 165 (2022) 141–157.

[24] J. Cook, L. Stefanski, Simulation-extrapolation estimation in parametric measurement error models, J. Am. Stat. Assoc. 89 (1994) 1314–1328.

[25] R. Carroll, D. Ruppert, L. Stefanski, C. Crainiceanu, Measurement Error in Nonlinear Models: A Modern Perspective, Chapman and Hall/CRC, 2006.

[26] M.D. Wilkerson, D.N. Hayes, ConsensusClusterPlus: a class discovery tool with confidence assessments and item tracking, Bioinformatics 26 (12) (2010) 1572–1573.

[27] Malika Charrad, Nadia Ghazzali, Véronique Boiteau, Azam Niknafs, NbClust: An R package for determining the relevant number of clusters in a data set, J. Stat. Softw. 61 (6) (2014).

[28] G. Yu, L.G. Wang, Y. Han, Q.Y. He, clusterProfiler: an R package for comparing biological themes among gene clusters, OMICS 16 (5) (2012) 284–287.

[29] M. Kanehisa, M. Furumichi, M. Tanabe, Y. Sato, K. Morishima, KEGG: new perspectives on genomes, pathways, diseases and drugs, Nucleic Acids Res. 45 (D1) (2017) D353–D361.

[30] N.M. Landry, S. Cohen, I.M.C. Dixon, Periostin in cardiovascular disease and development: a tale of two distinct roles, Basic Res. Cardiol. 113 (1) (2018) 1.

[31] Y. Kakimoto, C. Okada, N. Kawabe, A. Sasaki, H. Tsukamoto, R. Nagao, M. Osawa, Myocardial lipofuscin accumulation in ageing and sudden cardiac death, Sci. Rep. 9 (1) (2019) 3304.

[32] D.J. Crossman, A.A. Young, P.N. Ruygrok, G.P. Nason, D. Baddelely, C. Soeller, M. B. Cannell, T-tubule disease: relationship between t-tubule organization and regional contractile performance in human dilated cardiomyopathy, J. Mol. Cell. Cardiol. 84 (2015) 170–178.

[33] I.E. Setterberg, C. Le, M. Frisk, J. Li, W.E. Louch, The physiology and pathophysiology of T-tubules in the heart, Front. Physiol. 12 (2021), 718404.

[34] M. Ibrahim, J. Gorelik, M.H. Yacoub, C.M. Terracciano, The structure and function of cardiac t-tubules in health and disease, Proc. Biol. Sci. 278 (1719) (2011) 2714–2723.

[35] S. Brandenburg, J. Pawlowitz, F.E. Fakuade, D. Kownatzki-Danger, T. Kohl, G. Y. Mitronova, M. Scardigli, J. Neef, C. Schmidt, F. Wiedmann, F.S. Pavone, L. Sacconi, I. Kutschka, S. Sossalla, T. Moser, N. Voigt, S.E. Lehnart, Axial tubule junctions activate atrial Ca^{2+} release across species, Front. Physiol. 9 (2018) 1227.

[36] E. Wagner, S. Brandenburg, T. Kohl, S.E. Lehnart, Analysis of tubular membrane networks in cardiac myocytes from atria and ventricles, J. Vis. Exp. (92) (2014), e51823.

[37] E. Wagner, M.A. Lauterbach, T. Kohl, V. Westphal, G.S. Williams, J. H. Steinbrecher, J.H. Streich, B. Korff, H.T. Tuan, B. Hagen, S. Luther, G. Hasenfuss, U. Parlitz, M.S. Jafri, S.W. Hell, W.J. Lederer, S.E. Lehnart, Stimulated emission depletion live-cell super-resolution imaging shows proliferative remodeling of T-tubule membrane structures after myocardial infarction, Circ. Res. 111 (4) (2012) 402–414.

[38] D. Baddeley, I.D. Jayasinghe, L. Lam, S. Rossberger, M.B. Cannell, C. Soeller, Optical single-channel resolution imaging of the ryanodine receptor distribution in rat cardiac myocytes, Proc. Natl. Acad. Sci. U. S. A. 106 (52) (2009) 22275–22280.

[39] M.A. Clavel, J. Magne, P. Pibarot, Low-gradient aortic stenosis, Eur. Heart J. 37 (34) (2016) 2645–2657.

[40] J.S. Dahl, M.F. Eleid, H.I. Michelena, C.G. Scott, R.M. Suri, H.V. Schaff, P. A. Pellikka, Effect of left ventricular ejection fraction on postoperative outcome in patients with severe aortic stenosis undergoing aortic valve replacement, Circ. Cardiovasc. Imaging 8 (4) (2015).

[41] B.J. Maron, V.J. Ferrans, W.C. Roberts, Ultrastructural features of degenerated cardiac muscle cells in patients with cardiac hypertrophy, Am. J. Pathol. 79 (3) (1975) 387–434.

[42] A. Guo, C. Zhang, S. Wei, B. Chen, L.S. Song, Emerging mechanisms of T-tubule remodelling in heart failure, Cardiovasc. Res. 98 (2) (2013) 204–215.

[43] T. Seidel, S. Navankasattusas, A. Ahmad, N.A. Diakos, W.D. Xu, M. Tristani-Firouzi, M.J. Bonios, I. Taleb, D.Y. Li, C.H. Selzman, S.G. Drakos, F.B. Sachse, Sheet-like remodeling of the transverse tubular system in human heart failure impairs excitation-contraction coupling and functional recovery by mechanical unloading, Circulation 135 (17) (2017) 1632–1645.

[44] R.R. Kaprielian, S. Stevenson, S.M. Rothery, M.J. Cullen, N.J. Severs, Distinct patterns of dystrophin organization in myocyte sarcolemma and transverse tubules of normal and diseased human myocardium, Circulation 101 (22) (2000) 2586–2594.

[45] P. Asghari, D.R. Scriven, S. Sanatani, S.K. Gandhi, A.I. Campbell, E.D. Moore, Nonuniform and variable arrangements of ryanodine receptors within mammalian ventricular couplons, Circ. Res. 115 (2) (2014) 252–262.

[46] C. Franzini-Armstrong, F. Protasi, V. Ramesh, Shape, size, and distribution of Ca^{2+} release units and couplons in skeletal and cardiac muscles, Biophys. J. 77 (3) (1999) 1528–1539.

[47] Y. Hou, I. Jayasinghe, D.J. Crossman, D. Baddeley, C. Soeller, Nanoscale analysis of ryanodine receptor clusters in dyadic couplings of rat cardiac myocytes, J. Mol. Cell. Cardiol. 80 (2015) 45–55.

[48] D.J. Crossman, P.N. Ruygrok, C. Soeller, M.B. Cannell, Changes in the organization of excitation-contraction coupling structures in failing human heart, PLoS One 6 (3) (2011), e17901.

[49] N. Macquaide, H.T. Tuan, J. Hotta, W. Sempels, I. Lenaerts, P. Holemans, J. Hofkens, M.S. Jafri, R. Willems, K.R. Sipido, Ryanodine receptor cluster fragmentation and redistribution in persistent atrial fibrillation enhance calcium release, Cardiovasc. Res. 108 (3) (2015) 387–398.

[50] M.A. Peterzan, W.T. Clarke, C.A. Lygate, H.A. Lake, J.Y.C. Lau, J.J. Miller, E. Johnson, J.J. Rayner, M.J. Hundertmark, R. Sayeed, M. Petrou, G. Krasopoulos, V. Srivastava, S. Neubauer, C.T. Rodgers, O.J. Rider, Cardiac energetics in patients with aortic stenosis and preserved versus reduced ejection fraction, Circulation 141 (24) (2020) 1971–1985.

[51] C. Chimenti, A. Frustaci, Contribution and risks of left ventricular endomyocardial biopsy in patients with cardiomyopathies: a retrospective study over a 28-year period, Circulation 128 (14) (2013) 1531–1541.

[52] N. Frey, B. Meder, H.A. Katus, Left ventricular biopsy in the diagnosis of myocardial diseases, Circulation 137 (10) (2018) 993–995.

[53] Y. Perez-Riverol, A. Csordas, J. Bai, M. Bernal-Llinares, S. Hewapathirana, D. J. Kundu, A. Inuganti, J. Griss, G. Mayer, M. Eisenacher, E. Perez, J. Uszkoreit, J. Pfeuffer, T. Sachsenberg, S. Yilmaz, S. Tiwary, J. Cox, E. Audain, M. Walzer, A. F. Jarnuczak, T. Ternent, A. Brazma, J.A. Vizcaino, The PRIDE database and related tools and resources in 2019: improving support for quantification data, Nucleic Acids Res. 47 (D1) (2019) D442–D450.